Tunable Type-II BiVO_{4}/g-C_{3}N_{4} Nanoheterostructures for Photocatalysis Applications

Jihua Zhang, Mingsen Deng, Yunan Yan, Tiejun Xiao, Wei Ren, and Peihong Zhang

Phys. Rev. Applied **11**, 044052 — Published 17 April 2019

DOI: 10.1103/PhysRevApplied.11.044052

Tunable type-II $BiVO_4$/g-C_3N_4 nano-heterostructures for photocatalysis applications

Jihua Zhang,[a] Mingsen Deng [a] , Yunan Yan[a], Tiejun Xiao[a], Wei Ren[b,*], and Peihong Zhang[c,†]

[a]Guizhou Provincial Key Laboratory of Computational Nano-Material Science, Guizhou Education University, Guiyang, 550018, China

[b] Department of Physics, and International Center of Quantum and Molecular Structures, Materials Genome Institute, Shanghai University, Shanghai 200444, China

[c]Department of Physics, University at Buffalo, State University of New York, Buffalo, New York 14260, USA

[*]renwei@shu.edu.cn
[†]pzhang3@buffalo.edu

$BiVO_4$/g-C_3N_4 heterostructures combing the advantages of bismuth vanadate and graphitic carbon nitride have recently emerged as a promising material system for photocatalytic applications. Further performance improvement will require in-depth understanding and fine tuning the near-edge electronic properties of these heterostructures. In this work, we have investigated the electronic properties, in particular the band edge states that control the optical and transport properties, of $BiVO_4$/g-C_3N_4 nano-heterostructures using the Heyd, Scuseria, and Ernzerhof (HSE) hybrid functional approach. Our results demonstrate that $BiVO_4$/g-C_3N_4 heterostructures have a desired type-II band alignment, which may greatly facilitate rapid separation of photogenerated carriers. We find that the $BiVO_4$ subsystem responsible for the robust and strong optical absorption observed experimentally. Our calculated absorption edge of about 2.5 eV agrees remarkably well with the experimental value of 2.45 eV. We have also investigated the effect of external electric field on the band edge states, band alignment, and the optical and fundamental band gaps of the $BiVO_4$/g-C_3N_4 heterostructures. The band edge states of the $BiVO_4$ and g-C_3N_4 subsystems respond very differently to the applied electric field, resulting in electric-field tunable band offsets and band gap of the $BiVO_4$/g-C_3N_4 heterostructures. The contrasting response of the fundamental and optical gaps to electric field suggests a novel avenue for future experimental optimization of the optical absorption and carrier separation dynamics of these heterostructures for photoelectrochemical catalysis applications.

I. INTRODUCTION

Semiconductor-based photocatalysis has received tremendous research attention in wake of concerns about global environmental pollution and energy crisis [1]. In the past few decades, several methods[2-4] have been developed to overcome the serious shortcomings of fast charge recombination and limited visible-light absorption of semiconductor photocatalysts. One of the most widely explored strategies is the use of photocatalytic heterojunctions[2,5-7]. Previous work[8,9] has demonstrated that the construction of two semiconductors with suitable electronic structures may exhibit superior photoactivity than single photocatalysts. In particular, a type II band alignment at the heterostructure interface can facilitate rapid separation of photogenerated electron−hole pairs, resulting in significantly improved photocatalytic performance.

Bismuth vanadate ($BiVO_4$) is one of the most promising photocatalytic materials for water oxidation[10-14] due to its moderate band gap, high optical absorption, and being abundance, low cost, and highly stable[15-18]. On the other hand, graphite-phase carbon nitride g-C_3N_4 also exhibits good visible-light response[19,20] and has attracted a great deal of scientific interest for its applications in photocatalytic water splitting[19,21-26] and organic pollutant degradation[27-31]. Therefore, it is plausible that the $BiVO_4$/g-C_3N_4 heterostructures[9,32-39], which combine the advantages of g-C_3N_4 and $BiVO_4$, might give rise to superior photocatalytic performance. Experimentally, it is found that the $BiVO_4$/g-C_3N_4 heterojunction with different weight ratios of g-C_3N_4 resulted in varying photocatalytic efficiency. For example, Kong *et al*. reported that a $BiVO_4$/g-C_3N_4 heterostructure (26.94 wt.% of $BiVO_4$) exhibits an excellent oxygen evolution rate of 750 μmol $h^{-1}g^{-1}$ under visible light irradiation, which represents a 129% increase compared to that of pristine $BiVO_4$, and a photonic efficiency of 19%[40]. Che and co-workers[41] concluded that a 50/50 mass ratio $BiVO_4$/g-C_3N_4 heterojunction was the best for photocatalysis, showing remarkably higher photocatalytic activities in degrading rhodamineB (RhB) compared with pure C_3N_4 or $BiVO_4$. Sui and co-workers[39] demonstrated that a $BiVO_4$/g-C_3N_4 heterojunction with 7 wt% g-C_3N_4 was seven times more efficient than pristine $BiVO_4$. On the other hand, Sun *et al.* [37] showed that a $BiVO_4$/g-C_3N_4 heterojunction with 3% $BiVO_4$ exhibited the highest photocatalytic efficiency. Therefore, it is clear that optimal $BiVO_4$/g-C_3N_4 heterostructures have not been identified and there is still much room for improving their photocatalytic efficiency.

To better understand the improved photocatalytic performance of the $BiVO_4$/g-C_3N_4 heterojunctions, it is important to carry out systematic studies of their electronic properties and how they may be tuned, for example, with different weight ratios of the sub-systems or with an external field. Theory is able to provide useful insight for understanding experimental results and guidance for experimental design of heterostructure for improved photocatalytic performance.

Experimentally, it is difficult to realize tunable band gap by controlling the weight ratio of g-C_3N_4 in the $BiVO_4$/g-C_3N_4 heterojunction. For example, Sui and co-workers[39] concluded that the optical band gaps of $BiVO_4$ and $BiVO_4$@g-C_3N_4 (with 3, 5, 7, 10 wt% g-C_3N_4) are basically the same (about 2.45 eV) since they observed little change to the absorption edge among the samples. Their conclusion is consistent with several other experimental results[33,38,42]. However, it is often desirable to tune the electronic properties of heterostructures for optimal performance in different applications and conditions, and applying electric field is one of most convenient and effective approaches. Indeed, Kan and coworkers[43] have demonstrated that the band gap of bilayer g-C_3N_4, thus the optical properties, can be easily tuned by an external electric field.

In this work, we first investigate the structural and electronic properties of the $BiVO_4$/g-C_3N_4 heterojunctions with different number of g-C_3N_4 layers. This study provides an in-depth understanding of the important electronic structures features such as band gap, band edge states, band alignment, and the effect of the g-C_3N_4 layer thickness on the electronic and structural properties of these structures. We then study the effects of the electric-field on the electronic structure and interfacial properties of the $BiVO_4$/g-C_3N_4 heterojunctions. We find that $BiVO_4$/g-C_3N_4 heterojunctions have a desired type-II band alignment and that the $BiVO_4$ subsystem is responsible for the robust optical gap observed in experiment. In addition, the fundamental (minimum) band gap of the $BiVO_4$/g-C_3N_4 heterojunction can be effectively tuned by applying an external E-field, and a transition from semiconductor to metal is observed; the optical band gap, on the other hand, remains rather robust, but can also be tuned between 2.05 to 2.55 eV with a moderate E-field. More interestingly, the greater the number of the g-C_3N_4 layers, the more effective the E-field in tuning the band gap becomes.

II. COMPUTATIONAL

Density functional theory (DFT) based first-principles calculations are performed using the projected augmented wave (PAW)[44] method implemented in the Vienna *ab initio* simulation package (VASP).[45,46] The Kohn-Sham one-electron states are expanded using the plane wave basis set with a kinetic energy cutoff of 500 eV. The Perdew-Burke-Ernzerhof (PBE)[47] exchange-correlation (XC) functional within the generalized gradient approximation (GGA) is employed for the geometrical optimization. Since the van der Waals (vdW) interaction is expected to be important in these layered structures, in this work, we adopted the DFT-D3(BJ)[48] method with a Becke and Johnson (BJ) damped[49,50] vdW correction.

Since the GGA approach usually underestimates the band gap of semiconductors, we use the screened hybrid functional of Heyd, Scuseria, and Ernzerhof (HSE) [51] for a more accurate description of the electronic structure. In this work, we use the HSE06 functional [51] with a screening parameter ω = 0.2Å^{-1} and a small mixing parameter α (α = 0.175) for the short-range Hartree-Fock exchange instead of the commonly used value of 0.25. Using these parameters (i.e., ω = 0.2Å^{-1} and α = 0.175), the calculated band gaps of isolated monolayer g-C_3N_4 (2.70 eV) and bulk $BiVO_4$ (2.45eV) compare well with experimental results (2.7 eV[22] for g-C_3N_4 and 2.5 eV[52] for bulk $BiVO_4$) and previous theory (2.7 eV[9,53] for g-C_3N_4 and 2.4 eV[54] for bulk $BiVO_4$).

We mention that one should be cautious when comparing the theoretical band gap calculated here with experiment since the measured band gap includes several renormalization effects[55,56], including (but not limited to) electron-phonon renormalization, lattice polarization, and spin-orbit coupling effects. However, accurate calculations of the quasiparticle band gaps are not the main focus of this work. We expect that the band gap renormalization effects do not change the main results of this work since we attempt to model the already renormalized gap and band alignments, which are reproduced reasonably (admittedly fortuitously) using the HSE functional with appropriately chosen the HF mixing parameter.

The Brillouin-zone (BZ) integration is carried out using the Monkhorst-Pack [57] sampling method with a density of 2×6×1 for the $BiVO_4$/g-C_3N_4 heterostructures. A vacuum layer of 15 Å is included to avoid the interaction between neighboring slabs.

The external electric field is introduced by adding a planar dipole layer in the middle of the vacuum layer in the periodic supercell[58] as implemented in VASP. The effects of the applied electric field on the atomic structure are neglected as they are very small. All atoms are fully relaxed until the maximum magnitude of the force acting on the atoms is smaller than 0.03 eV/Å. We define the positive direction of the E-field as pointing from $BiVO_4$ (010) to g-C_3N_4, as shown in the inset of Fig. 1(f).

Note that there is substantial lattice mismatch between $BiVO_4$ and g-C_3N_4. For the heterostructures studied in this work, we use the averaged lateral lattice constants (of the supercells) to minimize the strains on both subsystems to within ±3.5%. This strain introduces a small enhancement to the band gap of the $BiVO_4$ slab from 2.45 eV to about 2.7 eV. For the g-C_3N_4 over-layer, the strain and interfacial interaction cause the structure to buckle as shown in Fig. 1. The buckling effects significantly enhances the band gap of g-C_3N_4 to about 3.1 eV, to be compared with about 2.7 eV for the flat g-C_3N_4.

The imaginary part $\varepsilon_2(\omega)$ of the dielectric function $\varepsilon(\omega)$ is calculated using the standard formulation:

$$\varepsilon_2(\omega) = \frac{Ve^2}{2\pi\hbar m^2\omega^2}\int d^3k \sum_{n,n'} |< n\vec{k}\,|\vec{p}\,|\,n'\vec{k}>|^2 \; f_{n\vec{k}}(1-f_{n\vec{k}'})\delta(E_{n\vec{k}} - E_{n'\vec{k}} - \hbar\omega), \qquad (1)$$

where V is the cell volume, $\hbar\omega$ is the energy of the incident photon, $\vec{p}$ is the momentum operator, $|\,n\vec{k}>$ the electronic state, and $f_{n\vec{k}}$ is the Fermi occupation function. The real part $\varepsilon_1(\omega)$ is related to $\varepsilon_2(\omega)$ by the Kramer–Krönig transformation. The absorption coefficient $a(\omega)$ can be derived from $\varepsilon_1(\omega)$ and $\varepsilon_2(\omega)$ as follows[59]

$$\alpha(\omega) = \frac{\sqrt{2}\omega}{c}[\sqrt{\varepsilon_1^2(\omega)+\varepsilon_2^2(\omega)} - \varepsilon_1(\omega)]^{1/2}. \qquad (2)$$

III. RESULTS AND DISCUSSION

A. Structural properties

In order to reduce the in-plane lattice mismatch, the heterostructure models are created by placing the g-C_3N_4 layers with a $2\sqrt{3}\times 1$ supercell and different thickness onto a 12-layer-thick 3×1 $BiVO_4$ (010) slab. In addition, we use the averaged lattice constants of the subsystems for the heterostructure models to minimize the effects on the lattice mismatch. The bottom 6 layers of the $BiVO_4$ (010) slab are fixed at the bulk structure while the top 6 layers are allowed to relax. We will denote the single-layer, double-layer, and tri-layer g-C_3N_4 on $BiVO_4$ (010) surface models as $BiVO_4$/SL-g-C_3N_4, $BiVO_4$/BL-g-C_3N_4, and $BiVO_4$/TL-g-C_3N_4, which are illustrated in Figs. 1 (a), (c), (e), respectively. We have studied several nonequivalent structures, namely, four for $BiVO_4$/SL-g-C_3N_4, eight for $BiVO_4$/BL-g-C_3N_4, and sixteen for $BiVO_4$/TL-g-C_3N_4. The lowest energy structures of $BiVO_4$/SL-g-C_3N_4, $BiVO_4$/BL-g-C_3N_4, and $BiVO_4$/TL-g-C_3N_4 are shown in Fig. 1(b), (d), and (f), respectively. These low energy structures we found are by no means the most stable structures. However, our main results should not be affects significantly if slightly different structures are used. In the following, we will focus on these lowest energy structures. It should be pointed out that both I2/b and C2/c space groups are commonly used to describe the monoclinic scheelite structure of $BiVO_4$[14]. Here we use the C2/c space group notion. The (010) surface using the C2/c space group notation is equivalent to (001) surface using the I2/b notion, which has been shown to be the most stable one [60]. Ideally, theoretical studies of photocatalysis should consider surface hydration effects as adsorption of water may modify the surface electronic properties. In addition, hydration may also cause degradation of photocatalysts. The issue of hydration effects is beyond the scope of this study but definitely deserves further investigations.

In order to address the stability of the heterostructures, we define an interface adhesion energy:

$$E(\text{ad.}) = [E(\text{hetero}) - E(\text{g-C}_3\text{N}_4) - E(\text{BiVO}_4]/S, \qquad (3)$$

where E(hetero), E(g-C_3N_4), and E($BiVO_4$) are the total energies of the relaxed $BiVO_4$/g-C_3N_4 heterostructure, g-C_3N_4 (001), and $BiVO_4$ (010) slabs, respectively; S is the area of the interface. The calculated adhesion energies for $BiVO_4$/SL-g-C_3N_4, $BiVO_4$/BL-g-C_3N_4, and $BiVO_4$/TL-g-C_3N_4 heterostructures are -0.20 eV/Å^2, -0.25 eV/Å^2, and -0.18 eV/Å^2, respectively, suggesting that these structures are stable. These adhesion energies are consistent with those for g-C_3N_4 (001) on the Zn_2GeO_4 (110) surface (-0.18 eV/Å^2)[61] and graphene-coupled Bi_2WO_6 (010) surface (-0.18 eV/Å^2)[8]. It should be noted that the calculated adhesion energy is significantly greater than that for typical vdW systems such as graphite, suggesting that both physical and chemical effects contribute to the surface adhesion. However, chemical hybridization effects are rather weak and there are no chemical bonds formed at the interface.

After structural optimization, the g-C_3N_4 layers show considerable distortion, as shown in Fig. 1(b), (d) and (f). The structural distortions, in particular, the wavy distortion features, are due in part to the lattice mismatch, which is about 3%. The local distortions and the small interfacial distances, however, suggest significant interfacial chemical interactions at the interface, which is similar to the results for g-C_3N_4 (001)/$ZnWO_4$ (010) heterostructure[62] and bilayer-g-C_3N_4/MoS_2 heterostructure[53]. We would like to mention that the lattice mismatch has minimal effects on the electronic structures. The vertical separation between the g-C_3N_4 layer and the $BiVO_4$ (010) surface is 1.85Å (h_1 in Fig. 1(b)) for the $BiVO_4$/SL-g-C_3N_4 structure, 2.24Å (h_2 in Fig. 1(d)) for $BiVO_4$/BL-g-C_3N_4, and 1.89Å (h_3 in Fig. 1(f)) for $BiVO_4$/TL-g-C_3N_4. These interlayer separations are smaller than typical vdW interaction distance. For example, the interlayer separation is 2.89 Å for the graphene/g-C_3N_4 heterostructure[63] , 2.87 Å for g-C_3N_4/TiO_2(100)[64] and 3.16 Å for DL-g-C_3N_4/MoS_2[53]. The shorter interlayer distance implies a stronger interlayer interaction between the $BiVO_4$ and g-C_3N_4 layers.

B. Electronic structure and band alignment

Electronic structures of the $BiVO_4$/g-C_3N_4 heterostructures are calculated using the HSE06 screened hybrid functional method. Figure 2 shows the calculated total density of state (TDOS, shown in green in Fig. 2) of the heterostructures and the partial density of state (PDOS) for the subsystems $BiVO_4$ (shown in orange) and g-C_3N_4 (dark blue). The position of the valence band maximum (VBM) is place at zero for all three heterostructures for better comparison. The calculated band gaps of the $BiVO_4$/SL-g-C_3N_4, $BiVO_4$/BL-g-C_3N_4, and $BiVO_4$/TL-g-C_3N_4 heterostructures are 1.27eV, 1.24eV, and 1.37eV, respectively, indicating that the number of g-C_3N_4 layers has little effect on the heterojunction bandgap. The calculated band gap (~ 1.2 to 1.4 eV), however, is significantly smaller than the experimentally measured optical gap of about 2.45 eV[39]. We will address this issue in Section C.

Band alignment is very important in understanding the enhanced photocatalytic properties in these nano-heterojunctions since it controls the separation of photo-generated carriers, which can be conveniently obtained by plotting the partial DOS of the subsystems across the interfaces. Dashed lines in Fig. 2 indicate the VBM and CBM of the $BiVO_4$ and g-C_3N_4 subsystems, and the resulting band alignment diagrams are shown in Fig. 2(d). It is clear that all three heterostructures have a type-II[65,66] band alignment. Therefore, photo-generated lowest-energy electrons and holes will spontaneously separate in these structures, making them suitable for photocatalysis applications. Our theoretical results are consistent with experimental observation[33,34,38]. For comparison, we also show in Fig. 2(e) the band alignment diagrams calculated using the PBE functional. Although the band gap of the heterostructures are severely underestimated with the PBE functional, the qualitative features of the band alignments are similar to those calculated using the HSE functional. We would like to mention that calculating the band alignments of bulk solids typically involves several steps due to the need to line up the electrostatic potential of the individual bulk solids[67]. For finite systems, however, band alignments at the interface can be obtained by inspecting the atomic resolved density of states.

To gain further insight into the electronic properties of these heterostructures, we show in Fig. 3(a) atomically resolved projected DOS using $BiVO_4$/BL-g-C_3N_4 as a representative system. It is evident that the VBM state is primarily of N-2*p* character with some contribution from C-2*p* states while the CBM is mostly of V-3*d* character with a small admixture of O-2*p* states. A more vivid picture of these atomically (therefore spatially) distinct characters of the VBM and CBM states is shown with the real-space charge density plot of the VBM and CBM states [Fig. 3(b)]. These results clearly reveal that the CBM and VBM states are localized in different layers of the $BiVO_4$/g-C_3N_4 heterostructures, thus facilitating the separation of electrons and holes when photo-carries are generated. As a result, the undesirable rapid electron-hole recombination can be greatly suppressed in these structures. Similar results are found for other systems by Niu et al.[68]

C. Optical properties of $BiVO_4$/g-C_3N_4 heterostructures

As we have mentioned earlier, the experimentally measured optical gap is about 2.45 eV for the $BiVO_4$/g-C_3N_4 heterostructures whereas the calculated HSE minimum gap ranges from 1.2 to 1.4 eV. Therefore, there appears to be a significant discrepancy between theory and experiment. Although in principle the Kohn-Sham gap cannot be compared directly with the optical excitation gap, we still expect a better agreement with experiment considering that our HSE calculations reproduce well the experimental gap for both $BiVO_4$ and g-C_3N_4 subsystems. To this end, we have carried out optical absorption calculations for the $BiVO_4$/g-C_3N_4 heterostructures at the DFT (HSE) level. Figure 4 shows the calculated optical absorption coefficient for the three heterostructures studied in this work. Interestingly, our calculations predict a sharp absorption starting at about 2.5 eV, regardless of the number of the g-C_3N_4 layers, which agree remarkably well with the experimental result of 2.45 eV[39].

The significant difference between the calculated minimum (fundamental) band gap and the optical absorption gap can be understood with the projected DOS shown in Fig.2 and 3. As we have discussed in the previous section, the VBM states are mostly derived from the g-C_3N_4 subsystem whereas the CBM states are from $BiVO_4$. The optical dipole matrix elements between these spatially separated VBM and CBM states are greatly suppressed due to the minimal overlap between the initial and final state wave functions. It is evident that strong absorption occurs when the photon energy exceeds the band gap of $BiVO_4$, and the $BiVO_4$ subsystem is responsible for the optical absorption at 2.45 eV.

We would like to mention that for layered systems such as those studied here both the quasiparticle self-energy and excitonic effects are important because of the relatively weak screening in the system. Ideally, one needs to carry out higher level calculations[69] beyond DFT to compare with optical experiments. Interestingly, it was found that the quasiparticle self-energy and the excitonic effects largely cancel out as far as the minimum absorption gap is concern. Therefore, although the excitonic effects will strongly modify the features of the optical absorption spectrum, the overall optical band gap can be compared satisfactory with DFT based calculations.

D. Tuning the band edge states with electric field

The robust optical gap may be considered as an advantageous property of the $BiVO_4$/g-C_3N_4 heterostructures. On the other hand, it may also be desirable that this optical gap (shown in Fig. 4) as well as the fundamental gap (shown in Fig. 2) be tunable to suit different application needs. In this regard, the nearly constant optical and fundamental gap may become a drawback. Applying an external electric field is one of the most effective ways for tuning the electronic properties of nanostructures such as the heterostructures studied in this work.

We have investigated the effect of external electric field on the band edge states and the optical and fundamental band gap of the $BiVO_4$/g-C_3N_4 heterostructures. The external electric field (***E***) is applied perpendicularly to the layer plane, which is important in practical applications[43,70,71]. We mention that we neglect the additional lattice distortions due to the applied electric field since they are found to be very small in our study. For example, with an applied field of 0.6 V/Å, additional relaxation only amounts to about 2 meV/atom change in the calculated energy. The lack of a large permanent dipole moment of the model structure helps to explain the small structural distortion effects. The calculated permanent dipole along the direction of the applied electric field is only about 1.0 Debye for the whole $BiVO_4$/SL-g-C_3N_4 system. From comparison, that permanent dipole moment of a single LiF molecule is about 6.5 Debye. The evolution of the fundamental (minimum) band gap with the applied external electric field ***E*** for the three $BiVO_4$/g-C_3N_4 heterostructures is shown in Fig. 5. All three $BiVO_4$/g-C_3N_4 heterostructures show a similar electric field dependent of the fundamental band gap, with the band gap of the $BiVO_4$/TL-g-C_3N_4 structure showing the strongest field dependence. The band gap can be tuned between 0 and 2.1 eV with the electric field changing from -0.3 to 0.3 V/Å for the $BiVO_4$/TL-g-C_3N_4 structure. This widely tunable band gap with a moderate electric field makes these structures an ideal choice for applications where improved performance may be achieved through band gap optimization. In addition, the electric field induced semiconductor-metal transition may find new applications for these structures beyond photocatalysis such as switching devices.

Since the band edge states of the $BiVO_4$ and g-C_3N_4 subsystems have distinct characters, we expect that they respond differently to the applied electric field. Thus, not only the fundamental band gap but also the band offsets and optical absorption gap may be tuned by an electric field. Figure 6(a) illustrates how the band edge states of the subsystems $BiVO_4$ and g-C_3N_4 in the $BiVO_4$/TL-g-C_3N_4 structure vary with the electric field. There are a few interesting observations that deserve mentioning. Both the CBM and VBM of the $BiVO_4$ subsystem move higher with increasing electric field, indicating that the electric dipole of these states is opposite to the positive direction defined in Fig. 1. The small nonlinear behavior is a result of second-order effects. The band edge states of the g-C_3N_4 subsystem, on the other hand, show very different response to the electric field. The VBM of g-C_3N_4 does not shift appreciably with the electric field, indicating that this state has a negligible dipole moment. The CBM of g-C_3N_4, however, shows an interesting parabolic behavior around zero electric field, suggesting that second order effects play an important role.

The different response of the subsystem band edge states to the electric field also suggests field-tunable band offsets. Figure 6(b) shows the band gap (E_g), optical gap (band gap of $BiVO_4$, E_{g_BiVO4}) and the conduction and valence band offsets (ΔE_V and ΔE_C) of $BiVO_4$/TL-g-C_3N_4 as a function of the external electric field. Both band offsets decrease monotonically with increasing E field, and they can both be tuned from positive to negative values. The semiconductor-metal transition is a result of the lowering of the CBM state of $BiVO_4$ with negative electric field, which eventually merges with the VBM of the g-C_3N_4 subsystem. As we have shown in Fig. 4, $BiVO_4$ is mostly responsible for the optical absorption of the $BiVO_4$/g-C_3N_4 heterostructures. Our analysis of the electric-field dependent band edge states also suggests that the optical band gap (E_{g_BiVO4}) of these structures can be tuned with electric field from about 2.05 to 2.5 eV as shown in Fig. 6(b) (orange curve). Therefore, although the fundamental gap can be widely tuned from 0 to 2.1 eV with an external field changing from -0.3 to 0.3 V/Å, the optical gap remains rather robust.

IV. SUMMARY

In summary, we have carried out an in-depth analysis of the electronic properties, in particular, the band edge states that control the optical and transport properties, of the $BiVO_4$/g-C_3N_4 nano-heterostructures using the HSE hybrid density functional approach. The distinct atomic character of the band edge states clearly indicates a type-II band alignment in these structures, which is beneficial for the separation of photogenerated carriers. Although the fundamental gap (1.2 ~ 1.4 eV) of the $BiVO_4$/g-C_3N_4 heterostructures is considerably smaller than that of the $BiVO_4$ or g-C_3N_4 subsystem, we find that strong optical absorption starts at about 2.5 eV for all three heterostructures investigated in this work. This result agrees remarkably well with the experimental observation of robust optical absorption at 2.45 eV.

We have also studied the effect of external electric field on the band edge states, band alignment, and the optical and fundamental band gaps of the $BiVO_4$/g-C_3N_4 heterostructures. The band edge states of the $BiVO_4$ and g-C_3N_4 subsystems respond very differently with the applied electric field, resulting in electric-field tunable band offsets and band gap of the $BiVO_4$/g-C_3N_4 heterostructures. The fundamental gap can be widely tuned from over 2.0 eV to zero, suggesting an electric-field induced semiconductor-metal transition in these structures. The optical gap, although can also be tuned slightly by electric field from 2.0 to 2.5 eV, remains rather robust. This contrasting response of the fundamental and optical gap to electric field may be exploited in future experiments to optimize the optical absorption and carrier separation dynamics in these heterostructures for photoelectrochemical catalysis applications.

ACKNOWLEDGEMENTS

This research was supported in part by the National Natural Science Foundation of China (Grants No. 11547011, 51672171, and 11628407) and the Natural Science Foundation of Guizhou Province (Grants No. QKHJC[2016]1113, QHPT [2017]5790-02). Work at UB is supported by the US NSF under Grants No. DMR-1506669 and DMREF-1626967.

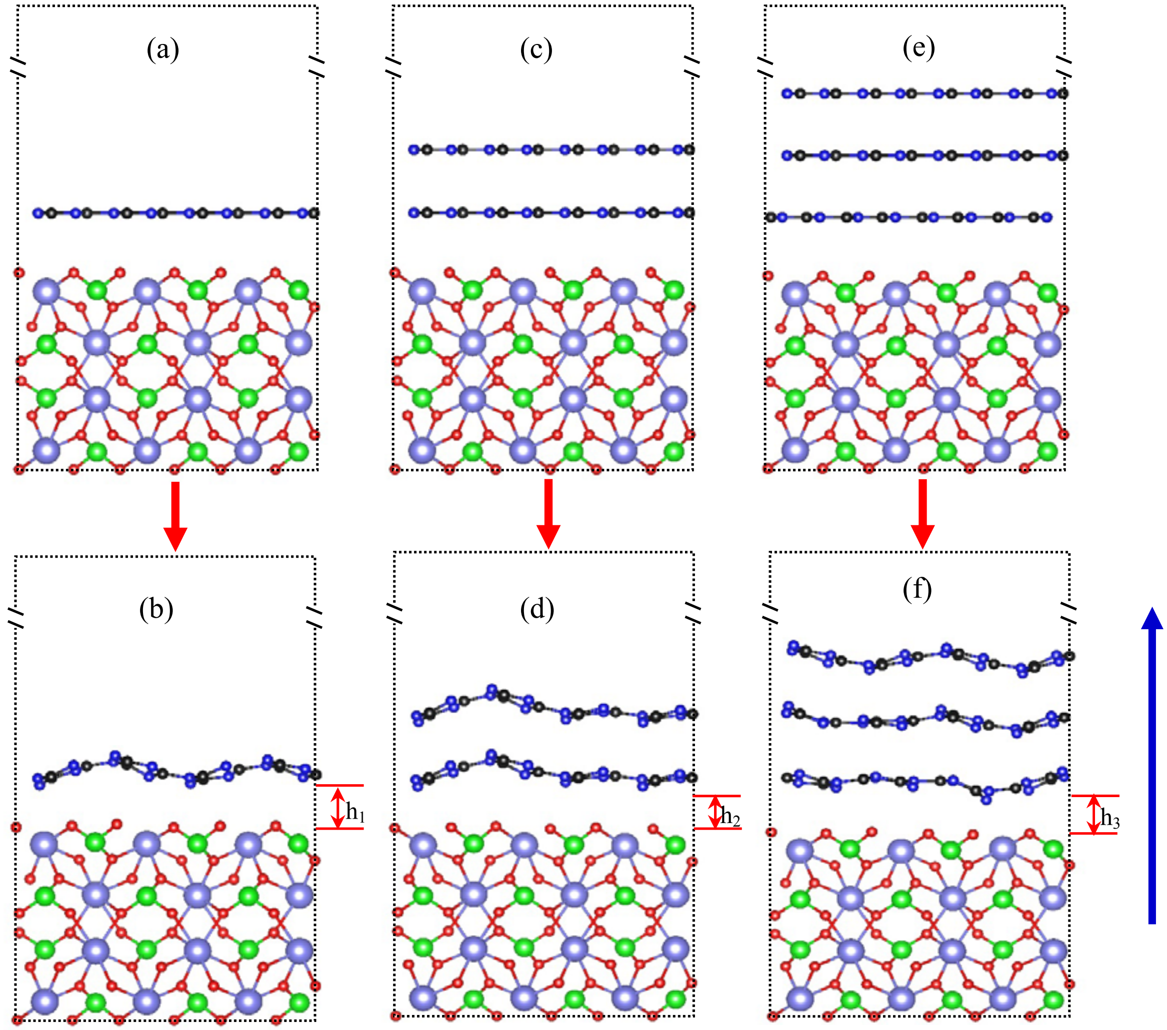

Fig. 1. Side view of the $BiVO_4/SL\text{-}g\text{-}C_3N_4$, $BiVO_4/BL\text{-}g\text{-}C_3N_4$, and $BiVO_4/TL\text{-}g\text{-}C_3N_4$ heterostructure: (a), (c), (e) are structures before optimization and (b), (d), (f) are after optimization, respectively. Red, green, light blue, blue and black balls represent O, V, Bi, N and C atoms, respectively. The blue arrows indicate the direction of the applied electric field.

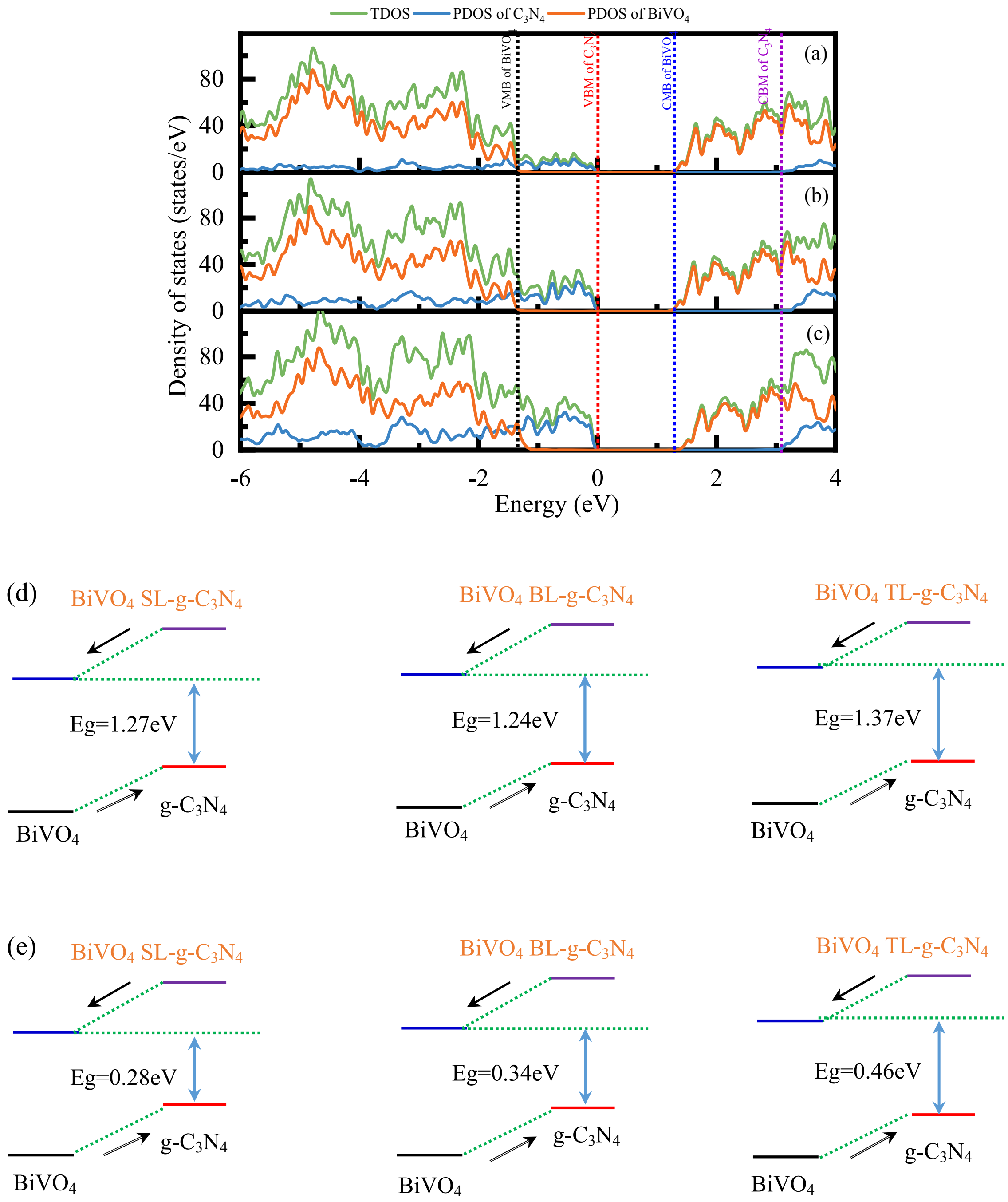

Fig. 2. Calculated TDOS and the corresponding PDOS of the C_3N_4 and $BiVO_4$ subsystems for (a) $BiVO_4$/SL-g-C_3N_4, (b) $BiVO_4$/BL-g-C_3N_4, and (c) $BiVO_4$/TL-g-C_3N_4 heterojunction using the HSE06 functional. (d) Band alignment of the heterojunctions obtained from the PDOS analysis using the HSE06 functional. (e) Band alignment obtained using the PBE functional. Relevant electronic parameters are also given in the figure. The position of the VBM is placed at zero for easy comparison.

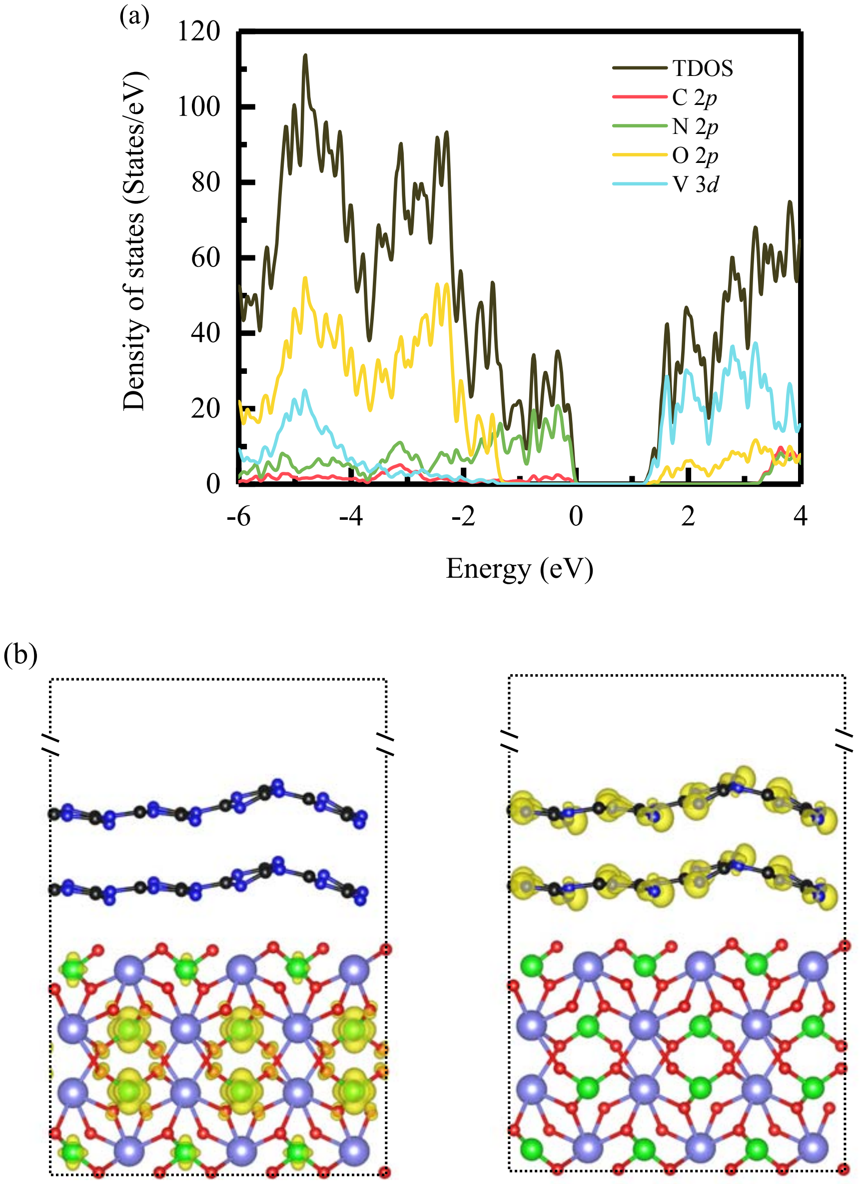

Fig. 3. (a) Calculated TDOS and atomically resolved PDOS of the $BiVO_4$/BL-g-C_3N_4 heterojunction using the HSE06 functional. Only dominant contributions from atomic states are shown in the figure. The VBM is place at zero. (b) Isosurface charge density plots for the CBM (left panel) and VBM (right panel) in $BiVO_4$/BL-g-C_3N_4 with an isosurface value of 0.02 e/au^2.

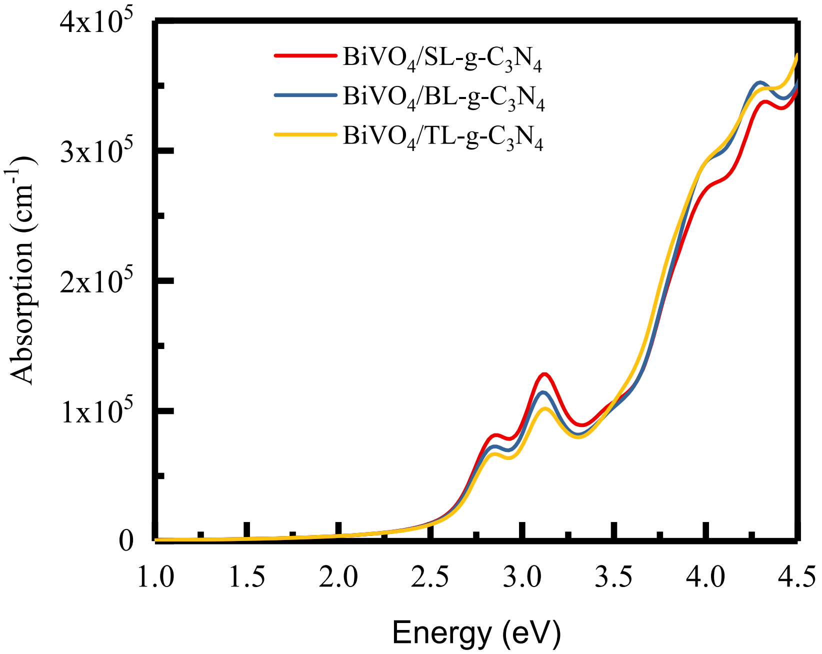

Fig. 4. Absorption coefficients of $BiVO_4/SL\text{-}g\text{-}C_3N_4$, $BiVO_4/BL\text{-}g\text{-}C_3N_4$, and $BiVO_4/TL\text{-}g\text{-}C_3N_4$ heterojunctions calculated using the HSE06 functional.

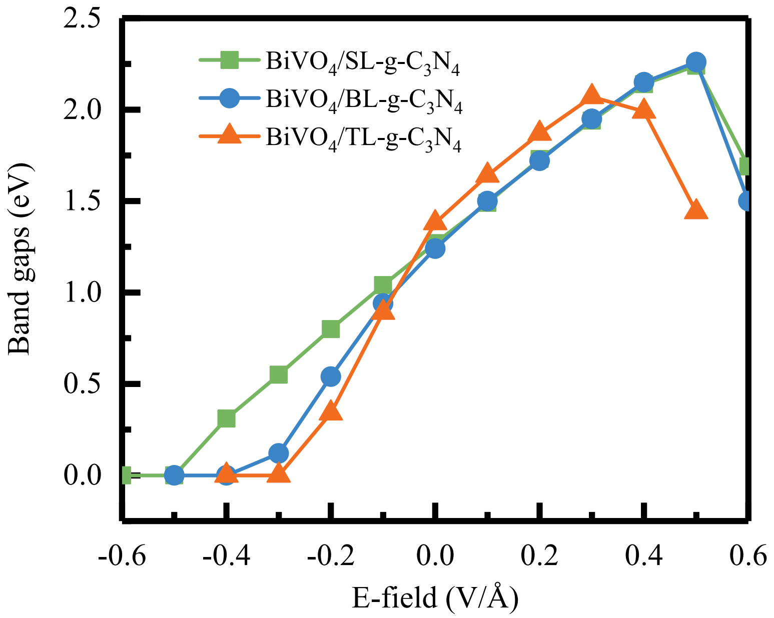

Fig 5. Calculated fundamental band gaps of $BiVO_4/SL\text{-}g\text{-}C_3N_4$, $BiVO_4/BL\text{-}g\text{-}C_3N_4$, and $BiVO_4/TL\text{-}g\text{-}C_3N_4$ heterostructure as a function of the external field.

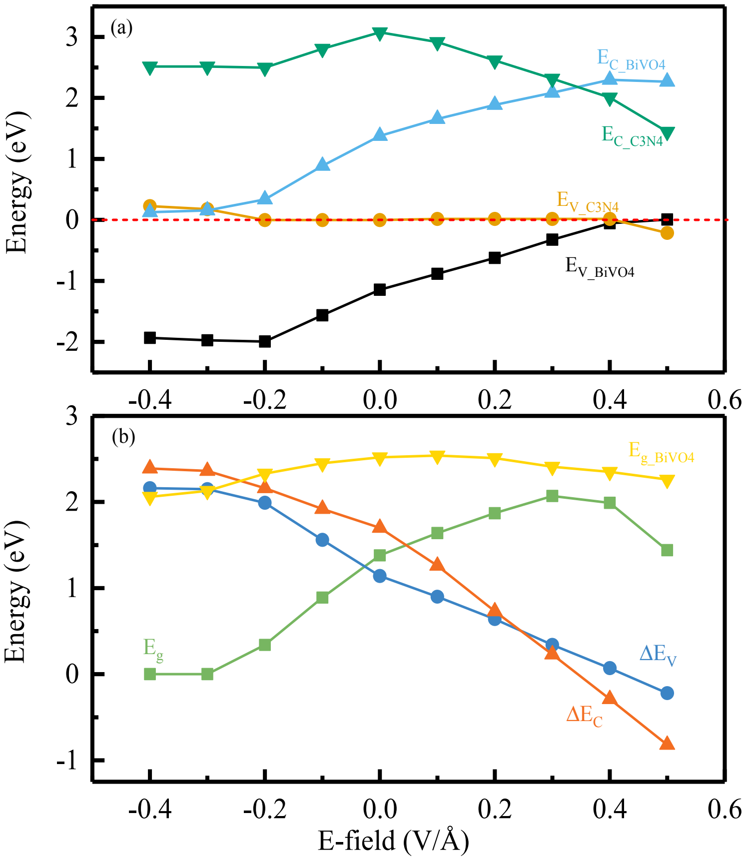

Fig. 6. (a) Band edge positions of the $BiVO_4$ and g-C_3N_4 subsystems in the $BiVO_4$/TL-g-C_3N_4 heterostructure as a function of the external field ***E***. E_{C_BiVO4} ($E_{C\_g\text{-}C3N4}$) and E_{V_BiVO4} ($E_{V\_g\text{-}C3N4}$) are the CBM and VBM of $BiVO_4$ (g-C_3N_4) in the $BiVO_4$/TL-g-C_3N_4 heterostructure. The position of the VBM at zero field is place at zero. (b) Evolution of the fundamental band gap (E_g), optical gap of the $BiVO_4$ subsystem (E_{g_BiVO4}) and the band offsets of $BiVO_4$/TL-g-C_3N_4 heterostructure as a function of the external field ***E***.

References

[1] H. Tong, S. Ouyang, Y. Bi, N. Umezawa, M. Oshikiri, and J. Ye, Nano-photocatalytic Materials: Possibilities and Challenges, Adv. Mater. **24**, 229 (2012).

[2] K. Sivula and R. van de Krol, Semiconducting Materials for Photoelectrochemical Energy Conversion, Nat. Rev. Mater. **1**, 15010 (2016).

[3] K. Maeda, Photocatalytic Water Splitting using Semiconductor Particles: History and Recent Developments, J. Photochem. Photobiol. C **12**, 237 (2011).

[4] X. Chen, S. Shen, L. Guo, and S. S. Mao, Semiconductor-based Photocatalytic Hydrogen Generation, Chem. Rev. **110**, 6503 (2010).

[5] H. Wang, L. Zhang, Z. Chen, J. Hu, S. Li, Z. Wang, J. Liu, and X. Wang, Semiconductor Heterojunction Photocatalysts: Design, Construction, and Photocatalytic Performances, Chem. Soc. Rev. **43**, 5234 (2014).

[6] S. Wang, J.-H. Yun, B. Luo, T. Butburee, P. Peerakiatkhajohn, S. Thaweesak, M. Xiao, and L. Wang, Recent Progress on Visible Light Responsive Heterojunctions for Photocatalytic Applications, J. Mater. Sci. Technol. **33**, 1 (2017).

[7] M. Bärtsch and M. Niederberger, The Role of Interfaces in Heterostructures, ChemPlusChem **82**, 42 (2017).

[8] F. Ren, J. Zhang, Y. Wang, and W. Yao, A Graphene-coupled Bi_2WO_6 Nanocomposite with Enhanced Photocatalytic Performance: a first-principles Study, Phys. Chem. Chem. Phys. **18**, 14113 (2016).

[9] J. Zhang, F. Ren, M. Deng, and Y. Wang, Enhanced Visible-light Photocatalytic Activity of a g-C_3N_4/$BiVO_4$ Nanocomposite: a first-principles Study, Phys. Chem. Chem. Phys. **17**, 10218 (2015).

[10] A. Kudo, K. Omori, and H. Kato, A Novel Aqueous Process for Preparation of Crystal Form-Controlled and Highly Crystalline $BiVO_4$ Powder from Layered Vanadates at Room Temperature and Its Photocatalytic and Photophysical Properties, J. Am. Chem. Soc. **121**, 11459 (1999).

[11] A. Kudo, K. Ueda, H. Kato, and I. Mikami, Photocatalytic O_2 Evolution Under Visible Light Irradiation on $BiVO_4$ in Aqueous $AgNO_3$ Solution, Catal. Lett. **53**, 229 (1998).

[12] N. Aiga, Q. Jia, K. Watanabe, A. Kudo, T. Sugimoto, and Y. Matsumoto, Electron–Phonon Coupling Dynamics at Oxygen Evolution Sites of Visible-Light-Driven Photocatalyst: Bismuth Vanadate, J. Phys. Chem. C **117**, 9881 (2013).

[13] H. W. Jeong, T. H. Jeon, J. S. Jang, W. Choi, and H. Park, Strategic Modification of $BiVO_4$ for Improving Photoelectrochemical Water Oxidation Performance, J. Phys. Chem. C **117**, 9104 (2013).

[14] Y. Park, K. J. McDonald, and K. S. Choi, Progress in Bismuth Vanadate Photoanodes for use in Solar Water Oxidation, Chem. Soc. Rev. **42**, 2321 (2013).

[15] Z. F. Huang, L. Pan, J. J. Zou, X. Zhang, and L. Wang, Nanostructured Bismuth Vanadate-based Materials for Solar-energy-driven Water Oxidation: a Review on Recent Progress, Nanoscale **6**, 14044 (2014).

[16] F. F. Abdi, N. Firet, and R. van de Krol, Efficient $BiVO_4$ Thin Film Photoanodes Modified with Cobalt Phosphate Catalyst and W-doping, ChemCatChem **5**, 490 (2013).

[17]M. S. Prévot and K. Sivula, Photoelectrochemical Tandem Cells for Solar Water Splitting, J. Phys. Chem. C **117**, 17879 (2013).

[18] P. Bornoz, F. F. Abdi, S. D. Tilley, B. Dam, R. van de Krol, M. Graetzel, and K. Sivula, A Bismuth Vanadate–Cuprous Oxide Tandem Cell for Overall Solar Water Splitting, J. Phys. Chem. C **118**, 16959 (2014).

[19] A. Thomas, A. Fischer, F. Goettmann, M. Antonietti, J.-O. Müller, R. Schlögl, and J. M. Carlsson, Graphitic Carbon Nitride Materials: Variation of Structure and Morphology and Their use as Metal-free Catalysts, J. Mater. Chem. **18**, 4893 (2008).

[20] W. J. Ong, L. L. Tan, Y. H. Ng, S. T. Yong, and S. P. Chai, Graphitic Carbon Nitride (g-C_3N_4)-Based Photocatalysts for Artificial Photosynthesis and Environmental Remediation: Are We a Step Closer To Achieving Sustainability?, Chem. Rev. **116**, 7159 (2016).

[21]X. Wang, K. Maeda, X. Chen, K. Takanabe, K. Domen, Y. Hou, X. Fu, and M. Antonietti, Polymer Semiconductors for Artificial Photosynthesis: Hydrogen Evolution by Mesoporous Graphitic Carbon Nitride with Visible Light, J. Am. Chem. Soc. **131**, 1680 (2009).

[22] X. Wang, K. Maeda, A. Thomas, K. Takanabe, G. Xin, J. M. Carlsson, K. Domen, and M. Antonietti, A Metal-free Polymeric Photocatalyst for Hydrogen Production from Water under Visible Light, Nat. Mater. **8**, 76 (2009).

[23] J. Hong, X. Xia, Y. Wang, and R. Xu, Mesoporous Carbon Nitride with in Situ Sulfur Doping for Enhanced Photocatalytic Hydrogen Evolution from Water under Visible Light, J. Mater. Chem. **22**, 15006 (2012).

[24] K. Takanabe, K. Kamata, X. Wang, M. Antonietti, J. Kubota, and K. Domen, Photocatalytic Hydrogen Evolution on Dye-sensitized Mesoporous Carbon Nitride Photocatalyst with Magnesium Phthalocyanine, Phys. Chem. Chem. Phys. **12**, 13020 (2010).

[25] H. Yan, Y. Chen, and S. Xu, Synthesis of Graphitic Carbon Nitride by Directly Heating Sulfuric Acid Treated Melamine for Enhanced Photocatalytic H_2 Production from Water under Visible Light, Int. J. Hydrogen Energy **37**, 125 (2012).

[26] K. Maeda, X. Wang, Y. Nishihara, D. Lu, M. Antonietti, and K. Domen, Photocatalytic Activities of Graphitic Carbon Nitride Powder for Water Reduction and Oxidation under Visible Light, J. Phys. Chem. C **113**, 4940 (2009).

[27] P. Niu, G. Liu, and H.-M. Cheng, Nitrogen Vacancy-Promoted Photocatalytic Activity of Graphitic Carbon Nitride, J. Phys. Chem. C **116**, 11013 (2012).

[28] J. Li, B. Shen, Z. Hong, B. Lin, B. Gao, and Y. Chen, A facile Approach to Synthesize Novel Oxygen-doped g-C_3N_4 with Superior Visible-light Photoreactivity, Chem. Commun. **48**, 12017 (2012).

[29] Y. Cui, Z. Ding, P. Liu, M. Antonietti, X. Fu, and X. Wang, Metal-free Activation of H_2O_2 by g-C_3N_4 under Visible Light Irradiation for the Degradation of Organic Pollutants, Phys. Chem. Chem. Phys. **14**, 1455 (2012).

[30] S. C. Yan, Z. S. Li, and Z. G. Zou, Photodegradation of Rhodamine B and Methyl Orange over Boron-Doped g-C_3N_4 under Visible Light Irradiation, Langmuir **26**, 3894 (2010).

[31] S. C. Yan, Z. S. Li, and Z. G. Zou, Photodegradation Performance of g-C_3N_4 Fabricated by Directly Heating Melamine, Langmuir **25**, 10397 (2009).

[32] D. Jiang, L. Chen, J. Zhu, M. Chen, W. Shi, and J. Xie, Novel p-n Heterojunction Photocatalyst Constructed by Porous Graphite-like C_3N_4 and Nanostructured BiOI: Facile Synthesis and Enhanced Photocatalytic Activity, Dalton trans. **42**, 15726 (2013).

[33] C. Li, S. Wang, T. Wang, Y. Wei, P. Zhang, and J. Gong, Monoclinic Porous $BiVO_4$ Networks Decorated by Discrete g-C_3N_4 Nano-islands with Tunable Coverage for Highly

Efficient Photocatalysis, Small **10**, 2783 (2014).

[34] J. Su, Z. Bai, B. Huang, X. Quan, and G. Chen, Unique three Dimensional Architecture using a Metal-free Semiconductor Cross-linked Bismuth Vanadate for Efficient Photoelectrochemical Water Oxidation, Nano Energy **24**, 148 (2016).

[35] F. Chen *et al.*, Novel Ternary Heterojunction Photcocatalyst of Ag Nanoparticles and g-C_3N_4 Nanosheets Co-modified $BiVO_4$ for Wider Spectrum Visible-light Photocatalytic Degradation of Refractory Pollutant, Appl. Catal. B **205**, 133 (2017).

[36] J. Cheng, X. Yan, Q. Mo, B. Liu, J. Wang, X. Yang, and L. Li, Facile synthesis of g-C3N4/BiVO4 heterojunctions with enhanced visible light photocatalytic performance, Ceram. Int. **43**, 301 (2017).

[37] R. Sun, Q. Shi, M. Zhang, L. Xie, J. Chen, X. Yang, M. Chen, and W. Zhao, Enhanced Photocatalytic Oxidation of Toluene with a Coral-like Direct Z-scheme $BiVO_4$/g-C_3N_4 Photocatalyst, J. Alloys Compd. **714**, 619 (2017).

[38] Y. Wang, J. Sun, J. Li, and X. Zhao, Electrospinning Preparation of Nanostructured g-C_3N_4/$BiVO_4$ Composite Films with an Enhanced Photoelectrochemical Performance, Langmuir **33**, 4694 (2017).

[39] Z. Zhang, M. Wang, W. Cui, and H. Sui, Synthesis and Characterization of a Core–shell $BiVO_4$@g-C_3N_4 Photo-catalyst with Enhanced Photocatalytic Activity under Visible Light Irradiation, RSC Adv. **7**, 8167 (2017).

[40] H. J. Kong, D. H. Won, J. Kim, and S. I. Woo, Sulfur-Doped g-C_3N_4/$BiVO_4$ Composite Photocatalyst for Water Oxidation under Visible Light, Chem. Mater. **28**, 1318 (2016).

[41] F. Guo, W. Shi, X. Lin, and G. Che, Hydrothermal Synthesis of Graphitic Carbon Nitride–$BiVO_4$ Composites with Enhanced Visible Light Photocatalytic Activities and the Mechanism Study, J. Phys. Chem. Solids **75**, 1217 (2014).

[42] N. Tian, H. Huang, Y. He, Y. Guo, T. Zhang, and Y. Zhang, Mediator-free Direct Z-scheme Photocatalytic System: $BiVO_4$/g-C_3N_4 Organic-inorganic Hybrid Photocatalyst with Highly Efficient Visible-light-induced Photocatalytic Activity, Dalton trans. **44**, 4297 (2015).

[43] F. Wu, Y. Liu, G. Yu, D. Shen, Y. Wang, and E. Kan, Visible-Light-Absorption in Graphitic C_3N_4 Bilayer: Enhanced by Interlayer Coupling, J. Phys. Chem. Lett. **3**, 3330 (2012).

[44] G. Kresse and D. Joubert, From Ultrasoft Pseudopotentials to the Projector Augmented-wave Method, Phys. Rev. B **59**, 1758 (1999).

[45] G. Kresse and J. Hafner, Ab initio Molecular Dynamics for Liquid Metals, Phys. Rev. B **47**, 558 (1993).

[46] G. Kresse and J. Furthmuller, Efficient Iterative Schemes for ab initio Total-energy Calculations using a Plane-wave Basis Set, Phys. Rev. B **54**, 11169 (1996).

[47] J. P. Perdew, K. Burke, and M. Ernzerhof, Generalized Gradient Approximation Made Simple, Phys. Rev. Lett. **77**, 3865 (1996).

[48] S. Grimme, S. Ehrlich, and L. Goerigk, Effect of the Damping Function in Dispersion Corrected Density Functional Theory, J. Comput. Chem. **32**, 1456 (2011).

[49] E. R. Johnson and A. D. Becke, A post-Hartree-Fock Model of Intermolecular Interactions: Inclusion of Higher-order Corrections, J. Chem. Phys. **124**, 174104 (2006).

[50] A. D. Becke and E. R. Johnson, Exchange-hole Dipole Moment and the Dispersion

Interaction, J. Chem. Phys. **122**, 154104 (2005).

[51] J. Heyd, G. E. Scuseria, and M. Ernzerhof, Hybrid Functionals Based on a Screened Coulomb Potential, J. Chem. Phys. **118**, 8207 (2003).

[52] J. K. Cooper, S. Gul, F. M. Toma, L. Chen, Y.-S. Liu, J. Guo, J. W. Ager, J. Yano, and I. D. Sharp, Indirect Bandgap and Optical Properties of Monoclinic Bismuth Vanadate, J. Phys. Chem. C **119**, 2969 (2015).

[53] J. Wang, Z. Guan, J. Huang, Q. Li, and J. Yang, Enhanced Photocatalytic Mechanism for the Hybrid g-C_3N_4/MoS_2 Nanocomposite, J. Mater. Chem. A **2**, 7960 (2014).

[54] L. Zhang, M.-G. Ju, and W. Liang, Structural Characteristics and Photoinduced Carrier Behaviors of the Mixed-phase $BiVO_4$: a First-principles Theoretical Study, Theor. Chem. Acc. **135**, 134 (2016).

[55] J. Wiktor, I. Reshetnyak, F. Ambrosio, and A. Pasquarello, Comprehensive Modeling of the Band Gap and Absorption Spectrum of $BiVO_4$, Physical Review Materials **1** (2017).

[56] J. Wiktor, F. Ambrosio, and A. Pasquarello, Role of Polarons in Water Splitting: The Case of $BiVO_4$, ACS Energy Lett. **3**, 1693 (2018).

[57] H. J. Monkhorst and J. D. Pack, Special Points for Brillouin-Zone Integrations, Phys. Rev. B **13**, 5188 (1976).

[58] J. Neugebauer and M. Scheffler, Adsorbate-substrate and Adsorbate-adsorbate Interactions of Na and K Adlayers on Al(111), Phys. Rev. B **46**, 16067 (1992).

[59] S. Saha, T. P. Sinha, and A. Mookerjee, Electronic Structure, Chemical Bonding, and Optical Properties of Paraelectric $BaTiO_3$, Phys. Rev. B **62**, 8828 (2000).

[60] G.-L. Li, First-principles Investigation of the Surface Properties of Fergusonite-type Monoclinic $BiVO_4$ Photocatalyst, RSC Adv. **7**, 9130 (2017).

[61] L. Sun, Y. Qi, C. J. Jia, Z. Jin, and W. Fan, Enhanced Visible-light Photocatalytic Activity of g-C_3N_4/Zn_2GeO_4 Heterojunctions with Effective Interfaces Based on Band Match, Nanoscale **6**, 2649 (2014).

[62] L. Sun, X. Zhao, C.-J. Jia, Y. Zhou, X. Cheng, P. Li, L. Liu, and W. Fan, Enhanced Visible-light Photocatalytic Activity of g-C_3N_4–$ZnWO_4$ by Fabricating a Heterojunction: Investigation Based on Experimental and Theoretical Studies, J. Mater. Chem. **22**, 23428 (2012).

[63] X. Li, Y. Dai, Y. Ma, S. Han, and B. Huang, Graphene/g-C_3N_4 Bilayer: Considerable Band Gap Opening and Effective Band Structure Engineering, Phys. Chem. Chem. Phys. **16**, 4230 (2014).

[64] J. Liu, B. Cheng, and J. Yu, A new Understanding of the Photocatalytic Mechanism of the Direct Z-scheme g-C_3N_4/TiO_2 Heterostructure, Phys. Chem. Chem. Phys. **18**, 31175 (2016).

[65] R. Marschall, Semiconductor Composites: Strategies for Enhancing Charge Carrier Separation to Improve Photocatalytic Activity, Adv. Funct. Mater. **24**, 2421 (2014).

[66] S. N. F. M. Nasir, H. Ullah, M. Ebadi, A. A. Tahir, J. S. Sagu, and M. A. Mat Teridi, New Insights into Se/$BiVO_4$ Heterostructure for Photoelectrochemical Water Splitting: A Combined Experimental and DFT Study, J. Phys. Chem. C **121**, 6218 (2017).

[67] C. G. Van de Walle and R. M. Martin, Theoretical Study of Band Offsets at Semiconductor Interfaces, Phys. Rev. B **35**, 8154 (1987).

[68] X. Niu, Y. Li, H. Shu, X. Yao, and J. Wang, Efficient Carrier Separation in Graphitic Zinc

Oxide and Blue Phosphorus van der Waals Heterostructure, J. Phys. Chem. C **121**, 3648 (2017).

[69] D. Y. Qiu, F. H. da Jornada, and S. G. Louie, Environmental Screening Effects in 2D Materials: Renormalization of the Bandgap, Electronic Structure, and Optical Spectra of Few-Layer Black Phosphorus, Nano Lett. **17**, 4706 (2017).

[70] Q. Sun, G. Qin, Y. Ma, W. Wang, P. Li, A. Du, and Z. Li, Electric Field Controlled CO_2 Capture and CO_2/N_2 Separation on MoS_2 Monolayers, Nanoscale **9**, 19 (2017).

[71] J. Gao, G. Zhang, and Y. W. Zhang, Vastly Enhancing the Chemical Stability of Phosphorene by Employing an Electric Field, Nanoscale **9**, 4219 (2017).